

Monte Carlo simulation of the light curves of radioactively-powered transients

PHYS642 - Radiative Processes in Astrophysics

NICHOLAS VIEIRA

1. INTRODUCTION

Even though they originate in different systems, supernovae (SNe) and kilonovae (KNe) bear many resemblances, and may be modelled or simulated using similar physics. Crudely, SNe result from either thermal runaway due to accretion of mass onto a white dwarf in a binary star system, or the gravitational collapse of the core of a massive star as it exhausts its fuel and can no longer support itself (e.g. Arnett 1979, 1980, 1982). In both cases, the progenitor star explodes, and ejecta is launched away from the system at relativistic speeds (Chevalier 1976). The extreme energies in these systems are such that radioactive isotopes, and especially ^{56}Fe , ^{56}Ni , and ^{56}Co , are rapidly synthesized in large abundances in the ejecta (Arnett 1996; Magee et al. 2018). These radioactive isotopes decay, and their decay products are promptly thermalized by the surrounding ejecta, resulting in a bright transient which evolves in the ultraviolet (UV), optical, and infrared (IR) on timescales of weeks to months (Colgate & McKee 1969; Falk & Arnett 1977; Chatzopoulos et al. 2012). Extragalactic SNe have been observed in the thousands in the last two decades, allowing for robust population statistics, and are relatively well-understood.

KNe, in contrast, are likely produced by the merger of two neutron stars (NSs) or a neutron star and a black hole (BH) which live in a binary system. In such mergers, the extreme gravity of the system is sufficient to tidally disrupt any NSs in the binary (Lattimer & Schramm 1974; Rosswog 2005). This tidal disruption (and, in the case of a NS-NS merger, the collision of the two NS interfaces) launches the extremely neutron-rich material of the star(s) away from the system (Metzger et al. 2010; Fernández & Metzger 2013; Foucart et al. 2014; Metzger & Fernández 2014; Fernández et al. 2017, 2019). In this neutron-rich ejecta, radioactive isotopes of the rapid neutron capture (r -process) elements are promptly synthesized (e.g. Eichler et al. 1989; Li & Paczyński 1998; Freiburghaus et al. 1999). These r -process elements make up approximately half of the known elements heavier than Fe, and include elements such as Au, Pt, and U. These isotopes decay, and their decay products are thermalized (Barnes et al. 2016), producing a transient which exceptionally evolves

in the UV/optical/IR on timescales of hours to days, significantly faster than any other known transient at these wavelengths (Siebert et al. 2017).

The construction of advanced gravitational wave (GW) detectors such as those of the Laser Interferometer Gravitational-wave Observatory (LIGO), Virgo, and Kamioka Gravitational Wave Detector (KAGRA) in the last decade has opened a new window into these events by enabling the simultaneous detection of these mergers in both GWs and electromagnetic (EM) waves. The first unambiguous detection of a KN was made in August 2017, when an electromagnetic counterpart was associated with the NS-NS merger GW170817 detected in GWs by the LIGO and Virgo interferometers (Abbott et al. 2017a). EM observers saw:

- A short gamma-ray burst GRB170817A just 1.7s after the GW signal (Abbott et al. 2017b),
- An UV/optical/IR transient which precisely resembled the expected KN, fading rapidly in the bluer wavelengths on timescales of $\lesssim 1$ day and more gradually on timescales of 5 – 10 days in the near and far IR (see Villar et al. 2017 for a compilation of observations),
- And a radio/X-ray signal which is thought to be indicative of an outflow from the system, evolving on the timescale of months (Haggard et al. 2017; Ruan et al. 2018; Mooley et al. 2018; Nynka et al. 2018).

This event garnered the attention of virtually the entire astronomy and physics communities and ushered in the era of *multi-messenger astronomy* involving both photons and GWs. GW170817 remains, to date, one of the most intensely-studied astrophysical objects.

As LIGO, Virgo, and KAGRA undergo successive upgrades in sensitivity, new KNe detections are expected (Abbott et al. 2018). Furthermore, with the advent of the Legacy Survey of Space and Time (LSST, LSST Science Collaboration et al. 2009; Ivezić et al. 2019) of the Vera C. Rubin Observatory (VRO), it is anticipated that thousands of new SNe and potentially KNe will be discovered in the coming years. The present is therefore an excellent time to develop and improve our modelling

of these radioactively-powered transients (Khatami & Kasen 2019). Sophisticated modelling of KNe in particular will be crucial as new sources are detected. To this end, simulations of NS-NS/NS-BH mergers and the ensuing EM emission have received much attention in recent years. These models have built on the foundation laid by many years of work in the simulation of SNe. In particular, Monte Carlo methods for simulating the spectra, polarization, and light curves of SNe have proved to be useful (e.g. Lucy 1999, 2005; Kasen et al. 2006) and are being adapted for simulation of KNe (Bulla et al. 2015; Bulla 2019; Khatami & Kasen 2019). In this paper, I present a Monte Carlo code with the goal of synthesizing the light curve of a general radioactively-powered transient. I focus here on the conditions relevant for a KN, but the code can readily be adapted to SNe in the future.

The structure of this paper is as follows: in Section 2, I present the theory behind the radiative processes at work. In Section 3, I discuss the implementation of the Monte Carlo code to carry out these processes and produce a light curve. In Section 4, I discuss my results, and in Section 5, I summarize and conclude.

2. THEORY AND MODELLING

2.1. Radioactively-powered transients

A KN is a transient event powered by the radioactive decay of freshly-synthesized r -process elements in the neutron-rich ejecta surrounding the remnant of a NS-NS or NS-BH merger. The decay products of these r -process isotopes thermalize in the surrounding ejecta, producing a unique UV/optical/IR signature. The input heating rate from these elements can be described by the following fitting formula (Korobkin et al. 2012):

$$L_{\text{in}}(t) = C \cdot M_{\text{ej}} \left(0.5 - \pi^{-1} \arctan\left(\frac{t - t_0}{\sigma}\right) \right)^{1.3}, \quad (1)$$

where t is the time post-merger, $C = 4 \times 10^{18} \text{ cm}^2 \text{ s}^{-3}$, $t_0 = 1.3 \text{ s}$, and $\sigma = 0.11 \text{ s}$ are constants, and the mass M_{ej} is the mass of the ejecta, where we have made the implicit assumption that the ejecta is entirely composed of r -process elements. Heating is nearly constant for the first $\sim 1.3 \text{ s}$ post-merger as free neutrons form the r -process elements. These nuclei then begin to decay, and L_{in} follows a decaying power law (Metzger 2019).

It has been shown that assuming 100% thermalization efficiency leads to an overestimate of the KN's brightness at peak, and thus, a time-dependent thermalization efficiency must also be considered. An analytic fit to the total thermalization efficiency is used (Barnes et al.

2016):

$$\epsilon_{\text{th}}(t) = 0.36 \left[e^{-at} + \frac{\ln(1 + 2bt^d)}{2bt^d} \right], \quad (2)$$

where t is the time post-merger in *days*, and a, b, d are fitting parameters of order unity which depend on the ejecta mass M_{ej} and characteristic ejecta velocity v_{ej} . These parameters are tabulated in Barnes et al. (2016, their table 1) under the assumption of a randomly-oriented magnetic field in the ejecta. For ejecta masses and velocities which are not tabulated, linear interpolation is used to obtain the fitting parameters at these ejecta parameters. With a thermalization efficiency and radioactive heating rate defined, we can use the formalism of Chatzopoulos et al. (2012, their equation 3) for the bolometric luminosity of a radioactively-powered transient. Under the assumptions that (1) the initial photosphere radius at $t = 0$ is negligibly small, (2) the input *thermal* energy at $t = 0$ is also negligible, and (3) the ejecta is homologously expanding (free expansion), the formalism of Chatzopoulos et al. (2012) reduces to:

$$L_{\text{bol}}(t) = \frac{2}{t_d^2} \exp\left(\frac{-t^2}{t_d^2}\right) \int_0^t L_{\text{in}}(t') \epsilon_{\text{th}}(t') \exp\left(\frac{t'^2}{t_d^2}\right) t' dt', \quad (3)$$

where $t_d = \sqrt{2\kappa_{\text{ej}} M_{\text{ej}} / \beta v_{\text{ej}} c}$ is the diffusion timescale of the system, with κ_{ej} the wavelength-averaged opacity of the ejecta and $\beta = 13.8$ a parameter which depends on the geometry of the merger. In Equation 3, we have assumed spherical symmetry and a centrally-concentrated energy source. An example bolometric light curve for $\kappa_{\text{ej}} = 1.0 \text{ cm}^2 \text{ g}^{-1}$ and various ejecta masses/velocities is shown in Figure 9 (Appendix A).

The use of this luminosity is as follows: under the assumption that the photosphere of the KN is well-described by a blackbody, the radius R_{phot} and temperature T_{phot} of the photosphere can be described analytically, removing the need for computing the temperature throughout the Monte Carlo code which is discussed below. In particular, the time-dependent radius of the photosphere will be the “launching point” for the photon packets, and the temperature will be used to set the energy distribution from which the packets are drawn. We thus define the radius and temperature of the photosphere:

$$T_{\text{phot}}(t) = \max \left[\left(\frac{L_{\text{bol}}(t)}{4\pi\sigma_{\text{sb}}v_{\text{ej}}^2 t^2} \right)^{1/4}, T_c \right], \quad (4)$$

$$R_{\text{phot}}(t) = \begin{cases} v_{\text{ej}} t & \text{if } T_{\text{phot}} > T_c \\ \left(\frac{L_{\text{bol}}(t)}{4\pi\sigma_{\text{sb}}T_c^4} \right)^{1/2} & \text{if } T_{\text{phot}} \leq T_c \end{cases},$$

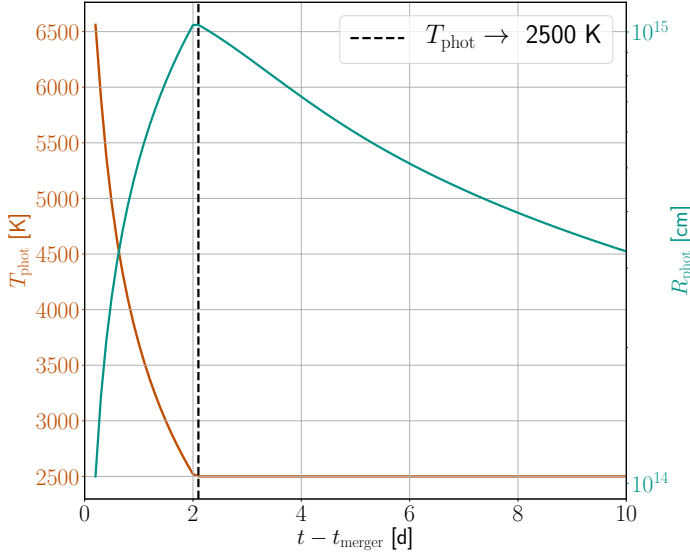


Figure 1. The radius R_{phot} and temperature T_{phot} of the photosphere over time. An ejecta mass of $M_{\text{ej}} = 0.02M_{\odot}$, a characteristic ejecta velocity of $v_{\text{ej}} = 0.2c$, and an average opacity of $\kappa_{\text{ej}} = 1.0 \text{ cm}^2 \text{ g}^{-1}$ are used. The temperature floor $T_c = 2500 \text{ K}$, near the recombination temperature of lanthanides. The radius of the photosphere is used at all points in the Monte Carlo to set the “launching point” of the photon packets, while the temperature sets the distribution of energies from which the photons are sampled.

where σ_{sb} is the Stefan-Boltzmann constant and we have defined a critical temperature floor T_c . Such a floor has been observed in many simulations of KNe, in the vicinity of $T_c \approx 2500 - 3000 \text{ K}$, and is likely related to the recombination temperature of the lanthanides (Barnes & Kasen 2013). We adopt $T_c = 2500 \text{ K}$. In this form, the photosphere expands homologously until the critical temperature is reached, at which point it begins to recede. An example of the evolution of the photosphere is shown in Figure 1, for parameters $M_{\text{ej}} = 0.02M_{\odot}$, $v_{\text{ej}} = 0.2c$, and $\kappa_{\text{ej}} = 1.0 \text{ cm}^2 \text{ g}^{-1}$. Under these conditions, the critical temperature is reached at $t \approx 2$ days and the photosphere expands to a maximum radius of $R_{\text{phot,max}} \approx 10^{15} \text{ cm}$.

To apply this model to a SNe rather than a KNe, one needs only to reassess the radioactive heating rate and, if applicable, the thermalization efficiency of this heating. Equation (3) is general and applies to all radioactively-powered transients.

2.2. Sources of opacity

The dominant sources of opacity which are seen by the photons as they launch from the photosphere and traverse the ejecta are electron scattering and bound-bound interactions. Bound-bound interactions in particular have a significant imprint on the light curve of a KN

due to the presence of the r -process elements. Crudely, due to (1) the increasing complexity in the atomic structure of the r -process elements with increasing atomic number Z , and (2) the presence of half-open f -shells in the lanthanides and actinides in particular, the density of atomic levels in r -process elements is much greater than that of e.g. ^{56}Fe , ^{56}Ni , or ^{56}Co in the ejecta of SNe (e.g. Tanaka et al. 2019, their figure 1). The effect of this density of lines, primarily in the optical and IR, is to make the r -process elements highly opaque to light at these wavelengths. An ejecta dominated by Fe-group elements such as SNe can have a wavelength-averaged opacity in the range of $\approx 10^{-3} - 10^{-1} \text{ cm}^2 \text{ g}^{-1}$, whereas the opacity of the r -process elements can reach up to $10^1 - 10^2 \text{ cm}^2 \text{ g}^{-1}$ (Tanaka et al. 2019). The key parameter which controls the opacity of some r -process mixture of elements is the electron fraction (or equivalently the proton fraction) Y_e of the material. A lower Y_e ejecta will contain more free neutrons, and will produce amongst the heaviest r -process elements, such as the lanthanides and actinides. Crudely, an ejecta with $Y_e \gtrsim 0.25$ will produce a blue, lanthanide-poor KN which peaks in the UV/optical on timescales of hours to days before rapidly fading, and an ejecta with $Y_e \lesssim 0.25$ will produce a red, lanthanide-rich KN which peaks and fades on longer timescales of \sim days in the optical/IR (Metzger 2019).

Unfortunately, with increasing atomic number, the nuclear physics data becomes woefully incomplete. To help remedy this, Tanaka et al. (2019) carried out systematic atomic structure calculations to produce opacities for *all* of the r -process elements. Following Bulla (2019), we combine these opacities to create an effective bound-bound opacity κ_{bb} which is both time- and wavelength-dependent. We define separate opacities for both a lanthanide-rich and a lanthanide-poor ejecta. The opacities follow (Bulla 2019; Tanaka et al. 2019):

$$\kappa_{\text{bb}}^{\text{lp}} = \begin{cases} 10^{2-4.3(\frac{\lambda}{10^4 \text{ \AA}})} \left(\frac{t}{t_0}\right)^{\gamma} \text{ cm}^2 \text{ g}^{-1} & \text{if } \lambda < 10^4 \text{ \AA} \\ 5 \times 10^{-3} \left(\frac{t}{t_0}\right)^{\gamma} \text{ cm}^2 \text{ g}^{-1} & \text{if } \lambda \geq 10^4 \text{ \AA} \end{cases},$$

$$\kappa_{\text{bb}}^{\text{lr}} = \begin{cases} 10^{2(1-\frac{\lambda}{10^4 \text{ \AA}})} \left(\frac{t}{t_0}\right)^{\gamma} \text{ cm}^2 \text{ g}^{-1} & \text{if } \lambda < 10^4 \text{ \AA} \\ 1.0 \left(\frac{t}{t_0}\right)^{\gamma} \text{ cm}^2 \text{ g}^{-1} & \text{if } \lambda \geq 10^4 \text{ \AA} \end{cases}, \quad (5)$$

for a lanthanide-poor ($Y_e \geq 0.25$) and lanthanide-rich ($Y_e < 0.25$) KN, respectively. $t_0 = 1.5$ days is a reference time and $\gamma = 1$. The opacity κ_{es} for electron scattering (which does not depend on λ or Y_e) is defined similarly

(Bulla 2019):

$$\kappa_{\text{es}} = 0.01 \left(\frac{t}{t_0} \right)^{-\gamma} \text{ cm}^2 \text{ g}^{-1}, \quad (6)$$

with the same definitions for t_0 and γ . Figure 2 shows the wavelength dependence of these opacities at a fixed time $t = 1.5$ days, as well as the ratio $\kappa_{\text{es}}/\kappa_{\text{bb}}$. (These figures are re-creations of figure 2 of Bulla 2019). Note that though both κ_{bb} increase linearly with t , at later times, the temperature of the ejecta drops (Figure 1) and thus the wavelengths of the photons being produced at the photosphere tend towards the red, suppressing the opacities following $\propto 10^{-\lambda}$ for $\lambda < 10^4$ Å.

In this paper, I have chosen to focus on a lanthanide-poor ejecta which produces a blue KN. The reason for this choice is that, as mentioned, the nuclear physics data becomes less complete and more uncertain for the heaviest of the r -process elements. Even if the work of Tanaka et al. (2019) allows us to circumvent opacity calculations, a line list is still needed to determine at which wavelengths photons will be involved in bound-bound interactions. Lines were compiled from the National Institute of Standards and Technology (NIST) Atomic Spectra Database (ASD)¹ and the Kurucz & Bell line list (Kurucz & Bell 1995)². A sample of the r -process elements with the greatest solar abundances (e.g. Ji et al. 2019, see their figure 1) are extracted from each list. The Kurucz line list contains many elements which are missing from the ASD (particularly the heavier elements) and contains far more lines than the ASD (> 50 million, in contrast with $\sim 200,000$ for the ASD). However, the ASD is more complete at the very shortest wavelengths, and so we use both lists. The elements which are selected from each are:

- NIST ASD: Ge ($Z = 32$), Rb (37), Sr (38), Y (39), Zr (40), Nb (41), Mo (42), Tc (43), Ru (44), Rh (45), Pd (46), Ag (47), Cs (55), Ba (56), Ir (76), Os (77), Pt (78)
- Kurucz: All of the above + Ga (31), Se (34), Te (52), La (57), Ce (58), Pr (59), Nd (60), Sm (62), Eu (63), Gd (64), Er (68), Au (79)

for a total of 29 elements considered. To ensure that computation times are not too long, only the strongest lines are selected. A cut on the oscillator strength of the ASD lines is applied, $f_{ik} \geq 0.05$, where i and k are the levels of the atom in question. Similarly, a cut of

¹ physics.nist.gov/PhysRefData/ASD/lines_form.html

² cfa.harvard.edu/amp/ampdata/kurucz23/sekur.html

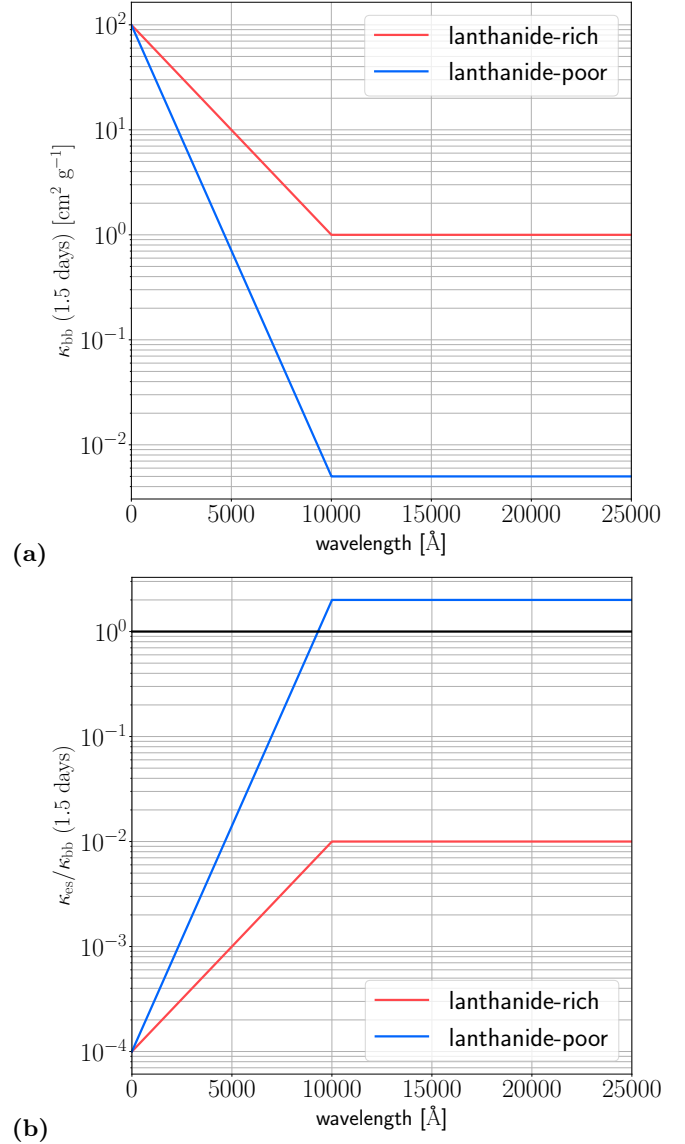


Figure 2. Wavelength-dependent bound-bound opacities at $t = 1.5$ days for a lanthanide-rich/lanthanide-poor ejecta, and their relation to electron scattering opacity. (a) Opacities are largest at UV/optical wavelengths for both lanthanide-rich and lanthanide-poor ejecta, sharply decreasing in IR. However, the presence of the lanthanides has a large impact on the opacity, especially at IR wavelengths. **(b)** For lanthanide-rich ejecta, electron scattering opacity is sub-dominant at all wavelengths. For lanthanide-poor ejecta, this holds only for wavelengths $\lesssim 8000$ Å, above which electron scattering and bound-bound transitions contribute equal amounts of opacity.

$\log_{10}(g_i f_{ik}) \geq -3$ (where $g_i = 2J_i + 1$) is applied to the Kurucz lines. For both databases, all sufficiently strong lines in the range of $0 - 25,000$ Å are obtained. As mentioned before, the ASD is more complete only at the shortest wavelengths. Therefore, a threshold wavelength 2200 Å is defined such that below this wavelength, the lines of the ASD are used, and above, the lines of Ku-

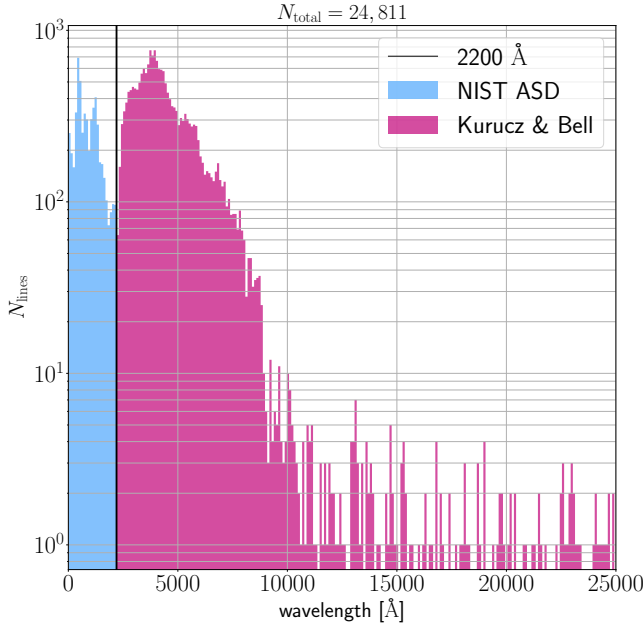


Figure 3. Lines acquired from the NIST ASD and the Kurucz & Bell line list. Below 2200 Å, lines are taken from the ASD, and above, lines are taken from Kurucz & Bell. This 2200 Å threshold was chosen to maximize the total number of lines.

curucz are used. This threshold was chosen to maximize the total number of lines (see Figure 10 in Appendix A for the number of lines obtained for various thresholds). A histogram of lines binned by wavelength is shown in Figure 3. A total number of 5489 NIST + 19,322 Kurucz = **24,811** lines are used. The density of lines is as expected from the opacity calculations of Tanaka et al. (2019), with an abundance of lines (and thus high opacity) at UV/optical wavelengths, and fewer lines (and thus less opacity) at IR wavelengths.

3. IMPLEMENTATION

The methods for implementation in this section are inspired primarily by the choices made in the following:

- POSSIS (Bulla et al. 2015; Bulla 2019)
- SEDONA (Kasen et al. 2006)
- The Monte Carlo code used in Mazzali & Lucy (1993)

These codes are *not* publicly available, and so the understanding of the code is based on their descriptions in the referenced studies. The code described here is available online at github.com/nvieira-mcgill/rad-transient. The script which actually runs the Monte Carlo is `rad_transient.py`. Other scripts are defined for various parts of the simulation, e.g. a script to compute heating rates and another to compute opacities. The

relevant scripts have been noted at the end of each of the following sections. The only script which is not mentioned is `lines.py`, which is used to submit an online query and download a line list from NIST ASD and to load in separately-downloaded Kurucz line lists.

3.1. Ejecta

An array of logarithmically-spaced concentric shells with radii r_i from $R_{\text{phot}}(t_{\text{init}})$ to $10 \times R_{\text{phot,max}}$ is used as the spatial grid for computation. As seen in Figure 1, $R_{\text{phot,max}} \approx 10^{15}$ cm, and so edge of the grid is set to 10^{16} cm. Each shell is assigned a velocity v_i and a density ρ_i . The velocity is that of homologous expansion, $v_i = r_i/t$. Following Bulla (2019), the density is described by:

$$\rho_{ij} = \rho_i(t_0) \left(\frac{t_j}{t_0} \right)^{-3}, \quad (7)$$

where j is a time-step and t_0 is some reference time. We adopt $t_0 = 1.5$ days, as in our description of the opacities. The density is initialized following Bulla (2019) as well:

$$\rho_i(t_0) = A r_i^{-\beta}, \quad (8)$$

where A is scaled to give the desired ejecta mass M_{ej} and $\beta = 3$, in line with the hydrodynamical simulations of e.g. Hotokezaka et al. (2013); Tanaka & Hotokezaka (2013). For the temperature profile, we assume that the temperature is uniform in the ejecta. The time-dependence of the temperature is therefore given in Equation (4). A more sophisticated model might consider a non-uniform temperature, but uniform-temperature models have had success in describing the evolution of the GW170817 KN (e.g. Villar et al. 2017). Moreover, we have assumed an electron fraction $Y_e > 0.25$ which is uniform throughout the ejecta. This is in general not true in both NS-NS and NS-BH mergers, which can produce multi-component KNe with e.g. a blue, lanthanide-poor ejecta near the poles of the system and a red, lanthanide-rich ejecta near the equator (Fernández & Metzger 2013; Fernández et al. 2017, 2019; Christie et al. 2019). This assumption could be removed in a more sophisticated version of this code.
Relevant scripts: `profiles.py`

3.2. Initializing photon packets

At each time step t_j , the energy injected into the system is computed:

$$E(t_j) = L_{\text{in}}(t_j) \epsilon_{\text{th}}(t_j) (t_j - t_{j-1}), \quad (9)$$

where $L_{\text{in}}(t_j)$ is the input radioactive heating rate, as defined in Equation (1), and $\epsilon_{\text{th}}(t_j)$ is the thermalization efficiency, as defined in Equation (2). This energy is

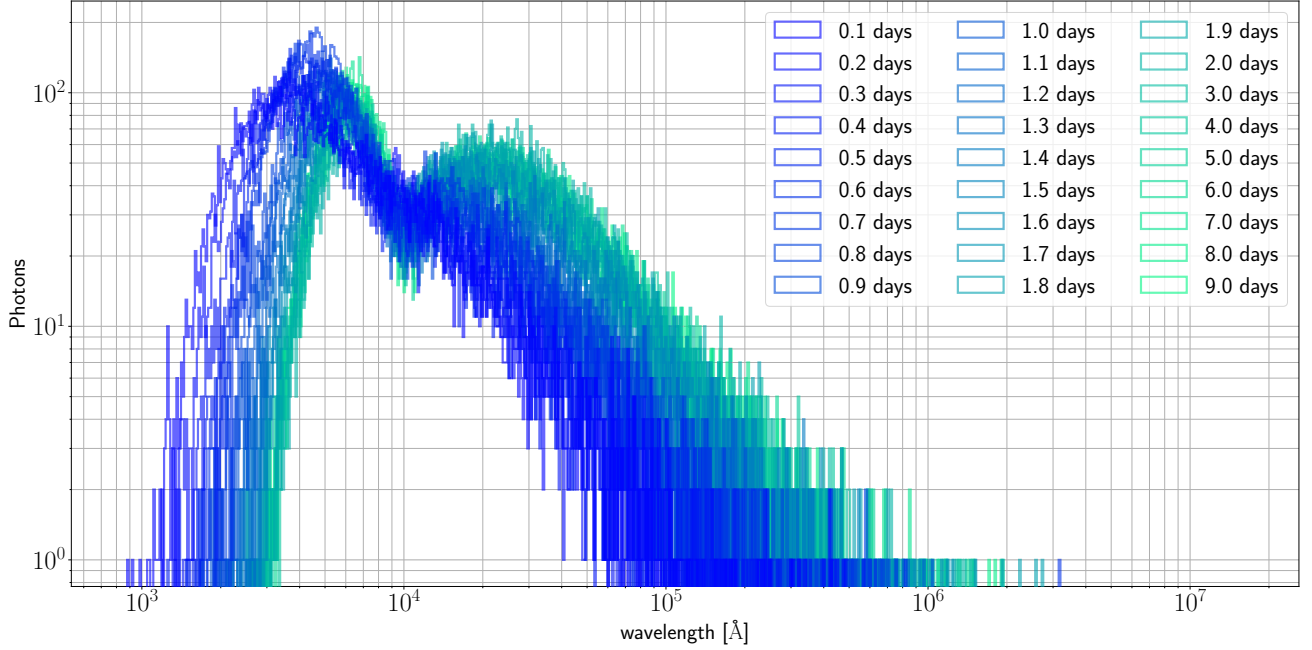


Figure 4. Histogram of the wavelengths of 10^4 photons sampled from the thermal emissivity. The thermal emissivity is described in Equation (10). The spectrum is approximately a blackbody, with a “dip” at 10^4 Å.

divided equally into N_{ph} *photon packets* such that each photon packet has an energy $e_{\text{ph}} = E(t_j)/N_{\text{ph}}$. The photons in each of these packets are identical. This technique of using equal-energy, indivisible photon packets as the quanta of the simulation has been widely-used in Monte Carlo approaches to SNe (e.g. Mazzali & Lucy 1993; Lucy 1999, 2005; Kasen et al. 2006), and in recent years, KNe (Bulla et al. 2015; Bulla 2019). The initial frequency of the photons which make up the packet is set by sampling the thermal emissivity, which follows (Bulla 2019):

$$S(\nu, T_j, t_j) = B(\nu, T_j) \kappa_{\text{tot}}(\nu, t_j), \quad (10)$$

where $B(\nu, T_j)$ is the Planck function describing a blackbody with temperature T_j and $\kappa_{\text{tot}}(\nu, t_j) = \kappa_{\text{es}}(t_j) + \kappa_{\text{bb}}(\nu, t_j)$ is the total opacity of the ejecta. A histogram of the wavelengths for 10^4 samples from this distribution is shown in Figure 4 at various times to show the time evolution of the spectrum. The spectrum gradually reddens over time, and does not undergo much evolution beyond $t = 2$ days, at which point the temperature floor $T_c = 2500$ K is reached in the ejecta. The spectrum mostly follows a blackbody, except for a “dip” at 10^4 Å = $1 \mu\text{m}$ (which is linked to our definition of the bound-bound opacities) which has been observed in the spectra of the GW170817 KN. Recent work has suggested that this dip may be strongly linked to the presence of strontium (Sr) in the ejecta (Watson et al. 2019). (We have included Sr as one of the light r -process elements in our line list).

The overall scheme for the Monte Carlo is then as follows:

1. Take a step in time to $t = t_j$. At t_j , compute the radius R_j and temperature T_j of the photosphere.
2. Draw a number N_{ph} of photon packets randomly from the thermal emissivity $S(\nu, T_j, t_j)$ (Equation (10)). Place these packets at a radius $r_i = R_j$, with an outgoing $\mu = \cos \theta_i$ (where θ_i is the angle of propagation with respect to the radial vector \hat{r}) which is sampled from $\mu = \sqrt{1 - z}$, such that the initial outgoing angle is isotropic but away from the photosphere, where z is drawn from the uniform distribution $\text{Unif}(0, 1)$.
3. For each photon packet n , which has wavelength λ_n and frequency ν_n which describes all of the identical photons in the packet, follow the scheme of Section 3.3 to determine whether the packet (1) scatters off of an electron, (2) interacts with a line, or (3) moves on to the next shell. For each interaction, compute the distance travelled and time elapsed *continuously* and add these to the location r_n (which begins at R_j) and t_n (which begins at t_j) of the photon packet. Determine the next interaction, and repeat until the photon packet exits the computational grid ($r_n \geq 10^{16}$ cm). If the packet is back-scattered beyond the initial photospheric radius from the beginning of the entire Monte Carlo ($r_n \leq R_{j=0}$), or if the time exceeds

the maximum escape time ($t_n \geq t_{j=\max(j)}$), treat the photon packet as being absorbed and therefore lost and unobserved.

4. Once all N_{ph} photon packets have escaped or have been lost, take another time step, and repeat Steps 1-3.

We now describe the scheme for selecting the event which occurs for each photon packet. *Relevant scripts: heating.py, distribs.py*

3.3. Event selection

The scheme for event selection follows that of [Mazzali & Lucy \(1993\)](#), who used a Monte Carlo approach to synthesize the spectra of SNe at early times. Note that primed (') quantities are in the co-moving frame (cmf), while unprimed quantities are in the rest frame. For the packet n of interest at radius r_n and time t_n , we compute the density $\rho_n = \rho(r_n, t_n)$ and the opacities $\kappa_{\text{bb},n} = \kappa_{\text{bb}}(\nu_n, t_n)$ and $\kappa_{\text{es},n} = \kappa_{\text{es}}(t_n)$. We then randomly draw an “event” optical depth τ_R from the distribution $\tau_R = -\ln(1-z)$, where z is again drawn from $\text{Unif}[0, 1]$. We then compare the optical depth τ_l of a line interaction and τ_{es} of electron scattering to τ_R . Specifically, we do the following:

1. Compute the length s_e which the packet can travel until $\tau_R = \tau_{\text{es}}$, i.e., $s_e = \tau_R/(\kappa_{\text{es}}\rho)$. This is the distance to electron scattering.
2. Transform λ_n in the rest frame to λ'_n in the cmf via a Doppler shift $\lambda'_n = \lambda_n(1 - \mu_n\beta_i)^{-1}$, where $\beta_i = v_i/c$ describes the velocity of the ejecta in the current (i^{th}) radial shell. Find the closest line λ_k in the line list which satisfies $\lambda_k \geq \lambda'_n$, if one exists. Compute the distance that the packet can travel until it interacts with this line as $s_{l,k} = ct_n(\lambda_k - \lambda'_n)/\lambda_k$. If no such line exists (i.e. $\lambda'_n > 25,000 \text{ \AA}$), send $s_{l,k} \rightarrow \infty$. This is the distance to a bound-bound interaction.
3. Compute the distance to the next shell, which will be at $r_{i+1} > r_i$ if the packet is travelling outwards in the ejecta ($\mu_n > 0$) or $r_{i-1} < r_i$ if the packet is travelling inwards ($\mu_n < 0$). The latter is possible if a previous scattering event has sent the packet inwards, as is discussed in Section 3.4. This distance $s_{\text{sh}} = \left| \frac{r_{\text{next}}}{\mu_n} \right|$ is the distance to exiting the shell without an interaction.
4. Find the minimum of s_e , $s_{l,k}$ and s_{sh} . If s_e is the minimum, propagate the packet a distance s_e

(equivalently, add $s_e\mu_n$ to r_n) and a time s_e/c , perform the electron scattering (Section 3.4) to determine the new direction and energy of the packet, and return to Step 1. If s_{sh} is the minimum, exit the shell altogether, propagating the packet a distance s_{sh} (equivalently, add $s_{\text{sh}}\mu_n$ to r_n) and a time s_{sh}/c , retain the propagation direction, and return to Step 1. Finally, if $s_{l,k}$ is the minimum, proceed to Step 5.

5. If $s_{l,k}$ is the minimum, we must now compare the optical depths τ_{es} , $\tau_{l,k}$, and τ_R . In computing the optical depth of the line, we make the *Sobolev approximation* that the line is sufficiently narrow that the packet interacts with the line only at a single frequency/wavelength. This is especially accurate in SNe ejecta (and even moreso in KNe ejecta) where the Doppler-broadened widths of the lines are much smaller than the length scales on which the ejecta properties vary ([Kasen et al. 2006](#)). If the total optical depth to interactions $\tau_{\text{tot}} = [\kappa_{\text{es},n}\rho_n]s_{l,k} + [\kappa_{\text{bb},n}\rho_n]s_{l,k}$ exceeds τ_R , immediately perform the line interaction as described in Section 3.5, compute the new propagation direction of the packet, propagate the packet a distance $s_{l,k}$ (equivalently, add $s_{l,k}\mu_n$ to r_n) and a time $s_{l,k}/c$, and return to Step 1. However, if this total optical depth does *not* exceed τ_R , move on to the next line $\lambda_{k+1} > \lambda_k$ and determine the total optical depth for the new distance $s_{l,k+1} > s_{l,k}$. Repeat this iteration m times until the total optical depth exceeds τ_R . If the distance $s_{l,k+m}$ exceeds s_{sh} or no m^{th} line exists, exit the shell and return to Step 1.

This process for event selection is repeated until the packet escapes the ejecta or is lost according to the conditions given in Section 3.2. The specifics in computing the outgoing energy and propagation direction of the packets are given in Section 3.4 for electron scattering events and Section 3.5 for bound-bound interaction events. *Relevant scripts: event_selection.py, doppler.py, opac.py*

3.4. Electron scattering

In this section and Section 3.5, we drop the n subscripts on various quantities for legibility.

In electron scattering, we first compute the outgoing propagation direction in the cmf ('). This is given by:

$$\mu'_{\text{out}} = \cos\theta'_{\text{out}} = \cos\alpha \cos\theta'_{\text{in}} - \sin\alpha \sin\theta'_{\text{in}} \cos\phi \quad (11)$$

where α is the scattering angle (which simplifies to $\theta'_{\text{out}} \pm \theta'_{\text{in}}$ in the case of scattering in a plane) and ϕ is the angle

around the cone of scattering. The relationship between angles in the rest frame and cmf (\cdot) is:

$$\mu' = \frac{\mu - v/c}{1 - \mu \cdot v/c}, \quad (12)$$

allowing for easy transformation from one frame to the other. The angle ϕ is uniformly distributed on $[0, 2\pi]$. The α angle, however, must be sampled from a probability distribution $\propto 1 + \cos^2 \alpha$. This is performed via a standard rejection method (Press et al. 1992, Section 7.3). With the correctly sampled angles, we can finally compute the outgoing energy of the scattered photon, which we assume scatters only once (Mazzali & Lucy 1993; Kasen et al. 2006):

$$e_{\text{out}} = e_{\text{out}} \frac{1 - \mu_{\text{in}} v/c}{1 - \mu_{\text{out}} v/c}, \quad (13)$$

in addition to the outgoing propagation cosine μ_{out} . These values are computed and the next event is selected. *Relevant script:* `electron_scattering.py`

3.5. Line scattering

In bound-bound interactions, we crudely model each line as a cavity in which the photon packet may become trapped, scattering one or more times, before escaping with a new energy and propagation direction. This model is based in part on the methods of Kasen et al. (2006), though we note that they consider other possible interactions with the line (absorption and fluorescence). The probability of a packet becoming trapped in a line is given by $1 - e^{-\tau_l}$, where $\tau_l = \kappa_{\text{bb}} \rho \cdot s_l$ is the previously determined optical depth of the line. We therefore once again draw a z from the distribution $\text{Unif}[0, 1)$, and the packet is trapped if $z < 1 - e^{-\tau_l}$. The packet scatters in the line, obtaining a new energy and propagation direction, and a new z is drawn to determine if the packet escapes, where the condition for escape is $z < \frac{1 - e^{-\tau_l}}{\tau_l}$. At each scattering, the outgoing propagation direction μ_{out} is sampled uniformly from $[0, 1)$, i.e., isotropically but outwards in the ejecta. The new rest-frame energy of the packet is then computed via Equation (13), and this scattering is repeated until the packet escapes. *Relevant script:* `line_scattering.py`

3.6. Packet collection

When the photons reach the edge of the computational grid, they are collected, and the energy, frequency, and arrival time are recorded. The outgoing angle is neglected in computing the radiation which is seen by the observer. This is not a good approximation, as the observer's viewing angle can strongly

impact the brightness and colour of a realistic, multi-component KN. A future version of the code could instead include this angular behaviour. *Relevant scripts:* `collect_results.py`, `collect_MC_info.py`

4. RESULTS AND DISCUSSION

The code described is relatively simple, but captures some of the features of both of the dominant radiative process occurring in the ejecta of SNe and KNe: electron scattering and bound-bound interactions. The required inputs for the code are, at minimum:

- The total ejecta mass M_{ej}
- The input heating rate $L_{\text{in}}(t)$, or some prescription for the energy which is distributed into photon packets at each time step
- A prescription for the time evolution of the radius $R_{\text{phot}}(t)$ of the photosphere and temperature $T(t)$ of the ejecta
- Electron scattering and bound-bound opacities κ_{es} and κ_{bb} , optionally (though not necessarily) wavelength and time-dependent
- A time-dependent density profile $\rho(r, t)$
- A line list

In our test of the code, we used the additional parameters of the characteristic velocity v_{ej} and wavelength-averaged grey opacity κ_{ej} as well, to compute L_{in} , the bolometric luminosity, and both $R_{\text{phot}}(t)$ and $T_{\text{phot}}(t)$.

In the following section, we show a simulated light curve of the KN for an ejecta mass $M_{\text{ej}} = 0.02 M_{\odot}$, ejecta velocity $v_{\text{ej}} = 0.2c$, and characteristic grey opacity $\kappa_{\text{ej}} = 1.0 \text{ cm}^2 \text{ g}^{-1}$. We impose a uniform electron fraction $Y_e = 0.4$ on all of the ejecta, although the precise value is arbitrary (since $Y_e > 0.25$, we use $\kappa_{\text{bb}}^{\text{lp}}$ of a lanthanide-poor ejecta, and Y_e does not figure anywhere else in our calculations). Our radial grid is composed of 100 concentric, logarithmically-spaced shells from $r = 8.6 \times 10^{13} \text{ cm}$ (the radius of the photosphere at $t = 0.1$ days) to 10^{16} cm . Time steps are also logarithmically-spaced, with 10 time steps from $t = 0.1$ days to 15 days.

For simplicity, we set $N_{\text{ph}} = 1$, such that running the Monte Carlo code once generates 10 time steps \times 1 packet per time step = 10 packets which may be collected. This lends itself well to parallelization, as is discussed in Section 4.2.

4.1. Light curve

The rate of escape of photon packets across all simulations is 81.2%, with the remaining packets being lost or

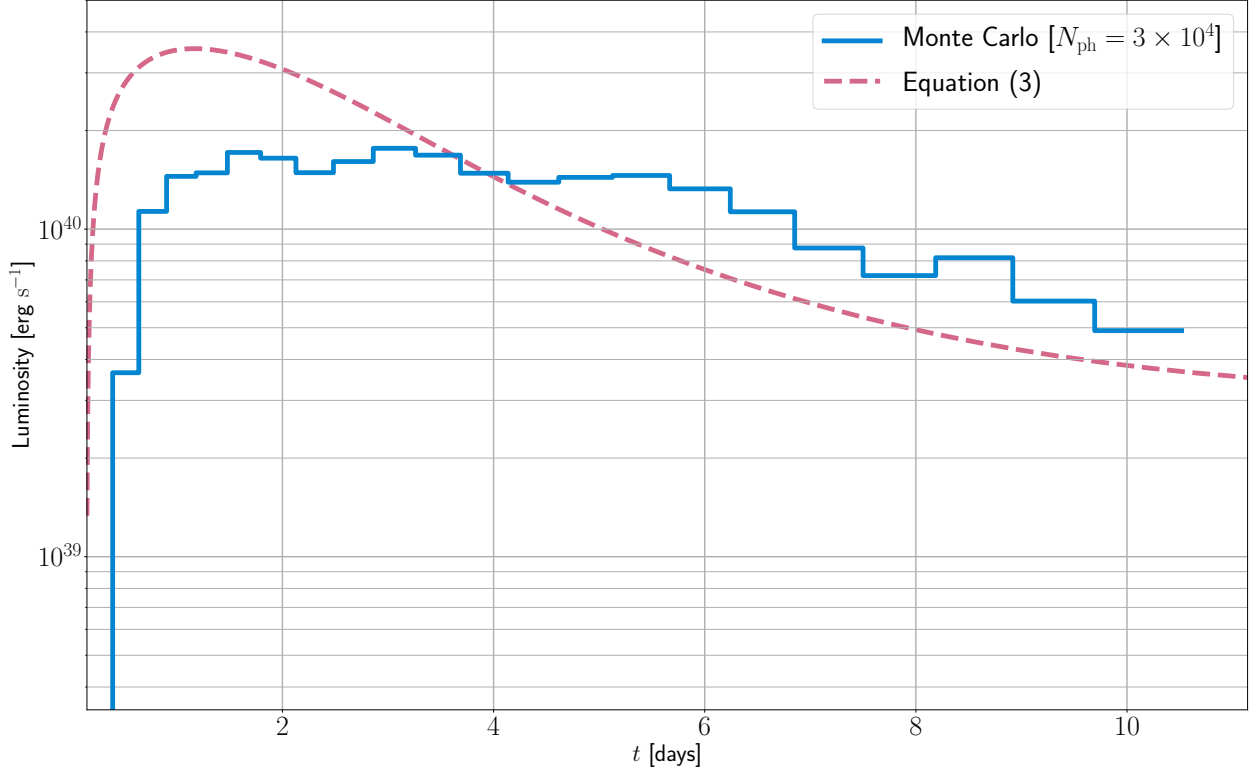


Figure 5. Light curve of the synthetic Monte Carlo light curve for a KN. A total of 3×10^4 photon packets are used in assembling the light curve. The luminosity is underestimated relative to the analytic result of Equation (3) by a factor of ~ 2 at peak, and fades at a slower rate than expected. Reasons for the failure of the Monte Carlo to capture the expected behaviour of the KN are discussed in Section 4.1.

absorbed. Our final tally of packets which successfully escape is $30,496 \approx 3 \times 10^4$. In Figure 5, we show a light curve constructed from the arrival times and final energies of each of these packets. Logarithmically-spaced time bins from 0 to 15 days each contain the sum of the energies which arrived in these bins, divided by the width of the bin to approximate a luminosity, and divided by the total number of packets. This light curve has been shifted leftward by a time of ~ 3.85 days, equal to the light crossing-time of 10^{16} cm in vacuum, for comparison with the analytic bolometric luminosity $L_{\text{bol}}(t)$ described in Equation (3).

Compared to the analytic result, our Monte Carlo underestimates the peak luminosity of the light curve by a factor of 2. Moreover, the rate of fading is slower than expected. There are several reasons why the Monte Carlo did not accurately reproduce a KN light curve. The relatively simple time and wavelength prescription for the opacities is unlikely to be the culprit, as these are the exact opacities used in Bulla (2019), which is able to accurately reproduce the light curve of the GW170817 KN. First and foremost, our treatment of line interactions is crude and only a starting point. A more sophisticated treatment including the possibility of e.g. absorption and fluorescence is necessary. In addition,

we have neglected other sources of opacity, bound-free and free-free interactions, which are sub-dominant compared to electron scattering and bound-bound processes but still play some role in the behaviour of the transient. We have also made the assumption that the electron fraction Y_e of the ejecta is uniform. This is not a valid assumption in most models of KNe, which contain two or even three distinct components in the ejecta, each with their own specific densities, geometric distribution, and characteristic electron fraction. This can be seen in Bulla (2019), which inspired many of the implementation choices made here, where they find that the GW170817 KN is well-described using a combination of a lanthanide-rich and lanthanide-poor component. Villar et al. (2017) similarly find that the GW170817 KN is best-fit by a three-component model. Finally, due to the limitations of the opacity calculations of Tanaka et al. (2019) at high T , we have begun our simulation at $t = 0.1$ days ($T \approx 7000$ K), at which point much of the UV emission may have already been produced. This additional emission at very early times might lead to better agreement between the Monte Carlo and the model at peak luminosity and would improve the agreement in the rate of fading.

4.2. Efficiency of the code

Despite the failure of the code to reproduce the expected light curve, we can assess the efficiency and speed of the code and look for sources of systematic error which might arise due to the computational techniques rather than physics of the models themselves.

The code was run primarily on the `irulan` server of McGill University. This server provides a total of 64 cores, each with approximately 1GB of RAM, which can be used in parallel. We run each Monte Carlo on a separate core. Figure 6 shows the average computation time for the entire Monte Carlo, i.e., the time during which the core is occupied. On average, a simulation with 10 time steps and 1 packet generated at each step takes ~ 40 s. The computation times are normally distributed around this mean, as might be intuitively expected. If all 64 cores are occupied, neglecting any “overhead” time required by the job submission queue in processing the simulations, this translates to ~ 6000 simulations, or a maximum of $\sim 60,000$ photon packets, in an hour. This number is smaller by about an order of magnitude for my personal laptop (8 cores, 1GB RAM/core).

We can also examine the computation time per packet, and compare the time required for packets which successfully escape the ejecta to those which do not. This comparison is shown in Figure 7. Interestingly, both the escaping and non-escaping packets show some degree of structure in when the computation terminates. The structure is also the same for both escaping and non-escaping packets, with peaks at 0.01 s and 10 s. The 0.01 s peak is by far the most significant. In the case of escaping packets, these computation times are likely representative of packets which were generated near the maximum radius of the photosphere and underwent very few interactions before escaping. For the non-escaping packets, these may be either (1) packets which were generated near the photospheric radius minimum, immediately back-scattered, and did not turn around to leave the ejecta before reaching the inner computational boundary ($\approx 8 \times 10^{13}$ cm), or (2) packets which were emitted at very late times, when the photosphere had receded, which did not make it to the outer computational boundary (10^{16} cm) before the end of the simulation at $t = 15$ days and were lost.

Finally, we examine the relationship between physical arrival time and Monte Carlo computation time for packets which escape in Figure 8. In general, it is expected that packets which undergo a greater number of scattering events take a longer time to compute, and also escape the ejecta at later times. This is seen in Figure 8. The 50% and 90% percentiles in arrival time are shown as vertical lines, demonstrating that the arrival

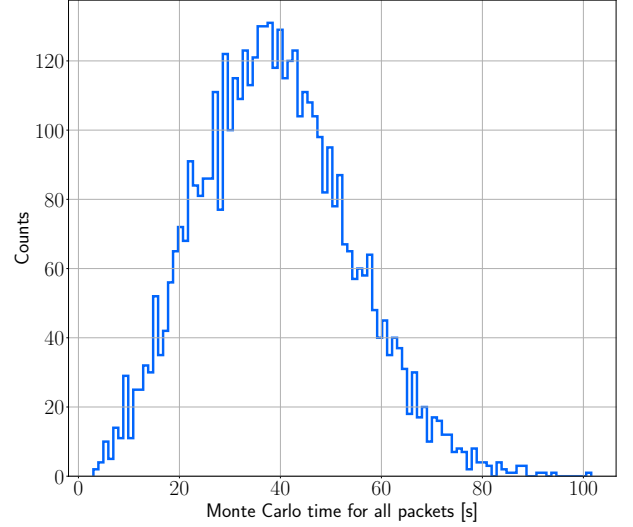


Figure 6. Computation times for each individual simulation. Each simulation employed 10 time steps and 1 photon packet generated at each step. Simulations were run on the `irulan` server of McGill University, with 1 simulation per core and 1GB RAM/core. An average Monte Carlo time of ~ 40 s is observed.

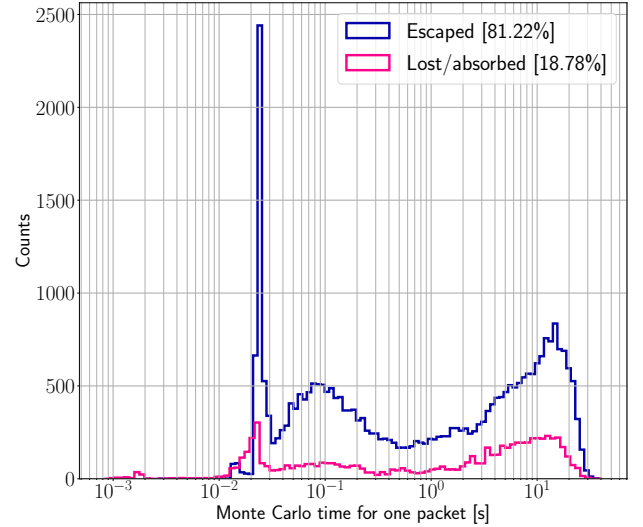


Figure 7. Computation times for each individual packet. Packets which escape and do not escape the ejecta both show similar structure, and in particular, peaks in the vicinity of 0.01s and 10s.

times are approximately uniformly distributed between the minimum possible time (the light-crossing time for 10^{16} cm, ~ 3.85 days) and the maximum allowed time (15 days, the end of the simulation). This uniform distribution might be responsible for the relative “flatness” of the light curve, and it is worth exploring if the additional UV emission mentioned in Section 4.1 would lead to a less uniform distribution, in the future.

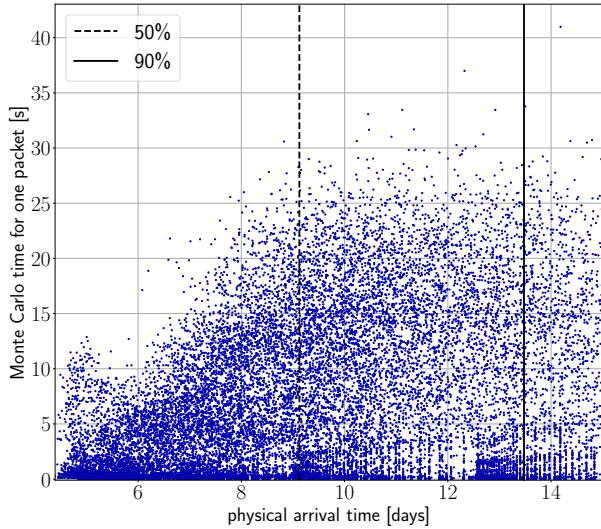


Figure 8. Comparison of the recorded arrival times and Monte Carlo computation times for packets which escape the ejecta. There is a general tendency towards later arrival times for packets which undergo a greater number of computations, as might be expected: packets which undergo many events will take longer to compute and will leave the ejecta at later times. Lines showing the 50% and 90% percentiles in arrival time are shown. Here, arrival times have *not* been offset by the light-crossing time of the computational grid.

4.3. Improvements

One of the possible improvements to the code would be to include an expansion opacity. In the formalism of Karp et al. (1977) and later Eastman & Pinto (1993), an expansion opacity can be used to combine the opacities of various sub-dominant lines (recall that we applied a cut on the strength of the lines to omit these) into an opacity grid. Explicitly, the absorption coefficient of this grid is given by (Kasen et al. 2006):

$$\alpha_{\text{exp}}(\lambda_c) = \frac{1}{ct} \sum_i \frac{\lambda_i}{\Delta\lambda_c} (1 - e^{-\tau_i}), \quad (14)$$

where λ_c is the central wavelength of a bin, $\Delta\lambda_c$ is the width of the bin (generally $\leq 10 \text{ \AA}$, Kasen et al. 2006), and the sum runs over all discrete lines of wavelength λ_i and optical depth τ_i . This would allow the code to include a larger number of isotopes and their lines with minimal impact on computation times, and would be especially useful in the interest of simulating a more red KNe, which involves the opacities of the heaviest of the r -process elements.

Regarding the radiative processes at work, the next major improvement would be a less crude treatment of bound-bound interactions. Presently, the model used neglects the possibility of a packet being completely absorbed during a transition, and neglects the possibility of the atom fluorescing (Kasen et al. 2006). In addition,

although they are sub-dominant, bound-free and free-free interactions have been completely neglected in this code. Bound-free interactions are expected to dominate over free-free, and so the former would be implemented first.

Finally, a proper treatment of the angular/geometric distribution of the electron fraction Y_e (which we assumed to be constant) and the incorporation of a viewing-angle into the binning of the output photon packets is necessary to produce the realistic, multi-component, asymmetric KNe which are naturally produced in full-fledged general relativity magnetohydrodynamical simulations.

5. CONCLUSIONS

We have developed a Monte Carlo code which makes the first step towards synthesizing the light curves of a general radioactive transient. The code considers only the dominant sources of opacity, electron scattering and bound-bound interactions, in determining the radiative processes which are at play. The code avoids explicitly solving the radiative transfer equation using a prescription for the time-evolution of the dominant opacities. We have applied this code to the test case of a lanthanide-poor, blue kilonova with reasonable ejecta parameters of $M_{\text{ej}} = 0.02 M_{\odot}$, $v_{\text{ej}} = 0.2c$, and $\kappa_{\text{ej}} = 1.0 \text{ cm}^2 \text{ g}^{-1}$. We find that the code does not accurately reproduce all of the features of a kilonova, and so we identify weaknesses of the code which could be remedied in the future and perform a brief search for systematic errors which might arise from computational techniques and not the actual physics involved.

REFERENCES

- Abbott, B. P., Abbott, R., Abbott, T. D., et al. 2017a, *ApJL*, 848, L12
- Abbott, B. P., Abbott, R., Abbott, T. D., et al. 2017b, *ApJL*, 848, L13
- Abbott, B. P., Abbott, R., Abbott, T. D., et al. 2018, *Living Reviews in Relativity*, 21, 3
- Arnett, W. D. 1979, *ApJL*, 230, L37
- Arnett, W. D. 1980, *ApJ*, 237, 541
- Arnett, W. D. 1982, *ApJ*, 253, 785
- Arnett, D. 1996, *Supernovae and Nucleosynthesis: An Investigation of the History of Matter*
- Barnes, J., Kasen, D. 2013, *AJ*, 775, 18
- Barnes, J., Kasen, D., Wu, M., Martínez-Pinedo, G. 2016, *AJ*, 829, 110
- Bulla, M., Sim, S. A., & Kromer, M. 2015, *MNRAS*, 450, 967
- Bulla, M. 2019, *MNRAS*, 489, 5037
- Chatzopoulos, E., Wheeler, J. C., Vinko, J. 2012, *AJ*, 746, 121
- Chevalier, R. A. 1976, *ApJ*, 207, 872
- Christie, I. M., Lalakos, A., Tchekhovskoy, A., et al. 2019, *MNRAS*, 490, 4811
- Colgate, S. A., & McKee, C. 1969, *ApJ*, 157, 623
- Eastman, R. G., & Pinto, P. A. 1993, *ApJ*, 412, 731
- Eichler, D., Livio, M., Piran, T., et al. 1989, *Nature*, 340, 126
- Falk, S. W., & Arnett, W. D. 1977, *ApJS*, 33, 515
- Fernández, R., & Metzger, B. D. 2013, *MNRAS*, 435, 502
- Fernández, R., Foucart, F., Kasen, D., et al. 2017, *Classical and Quantum Gravity*, 34, 154001
- Fernández, R., Tchekhovskoy, A., Quataert, E., et al. 2019, *MNRAS*, 482, 3373
- Foucart, F., Deaton, M. B., Duez, M. D., et al. 2014, *PhRvD*, 90, 024026
- Freiburghaus, C., Rosswog, S., & Thielemann, F.-K. 1999, *ApJL*, 525, L121
- Haggard, D., Nynka, M., Ruan, J. J., et al. 2017, *ApJL*, 848, L25
- Hotokezaka, K., Kyutoku, K., & Shibata, M. 2013, *PhRvD*, 87, 044001
- Ivezić, Ž., Kahn, S. M., Tyson, J. A., et al. 2019, *ApJ*, 873, 111
- Ji, A. P., Drout, M. R., & Hansen, T. T. 2019, *ApJ*, 882, 40
- Karp, A. H., Lasher, G., Chan, K. L., et al. 1977, *ApJ*, 214, 161
- Kasen, D., Thomas, R. C., & Nugent, P. 2006, *ApJ*, 651, 366
- Khatami, D. K., & Kasen, D. N. 2019, *ApJ*, 878, 56
- Korobkin, O., Rosswog, S., Arcones, A., Winteler, C., et al. 2012, *MNRAS*, 426, 3, 1940-1949
- Kurucz, R., & Bell, B. 1995, *Atomic Line Data* (R.L. Kurucz and B. Bell) Kurucz CD-ROM No. 23. Cambridge, 23
- Lattimer, J. M., & Schramm, D. N. 1974, *ApJL*, 192, L145
- Li, L.-X., & Paczyński, B. 1998, *ApJL*, 507, L59
- LSST Science Collaboration, Abell, P. A., Allison, J., et al. 2009, *arXiv e-prints*, arXiv:0912.0201
- Lucy, L. B. 1999, *A&A*, 344, 282
- Lucy, L. B. 2005, *A&A*, 429, 19
- Magee, M. R., Sim, S. A., Kotak, R., et al. 2018, *A&A*, 614, A115
- Mazzali, P. A., & Lucy, L. B. 1993, *A&A*, 279, 447
- Metzger, B. D., Martínez-Pinedo, G., Darbha, S., et al. 2010, *MNRAS*, 406, 4, 2650-2662
- Metzger, B. D., & Fernández, R. 2014, *MNRAS*, 441, 3444
- Metzger, B. D. 2019, *Living Rev Relativ*, 23, 1
- Mooley, K. P., Frail, D. A., Dobie, D., et al. 2018, *ApJL*, 868, L11
- Nynka, M., Ruan, J. J., Haggard, D., et al. 2018, *ApJL*, 862, L19
- Press, W. H., Teukolsky, S. A., Vetterling, W. T., et al. 1992, Cambridge: University Press
- Rosswog, S. 2005, *AJ*, 634, 1202
- Ruan, J. J., Nynka, M., Haggard, D., et al. 2018, *ApJL*, 853, L4
- Siebert, M. R., Foley, R. J., Drout, M. R., et al. 2017, *ApJL*, 848, L26
- Tanaka, M. & Hotokezaka, K. 2013, *AJ*, 775, 113
- Tanaka, M., Kato, D., Gaigalas, G., et al. 2019, *arXiv e-prints*, arXiv:1906.08914
- Villar, V. A., Guillochon, J., Berger, E., et al. 2017 *AJ*, 851, L21
- Watson, D., Hansen, C. J., Selsing, J., et al. 2019, *Nature*, 574, 497

APPENDIX

A. SUPPLEMENTAL PLOTS

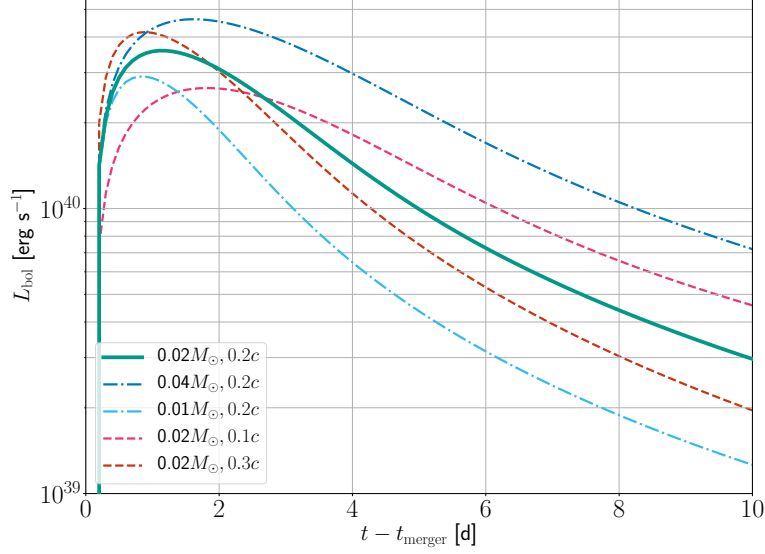


Figure 9. Bolometric KNe light curves for various ejecta masses and velocities, using the 1D, single-component model outlined in Section 2. Relative to the primary model (solid line), a heavier ejecta causes the KN to peak at later times and attain a greater peak luminosity. For faster ejecta, the KN peaks at earlier times and larger luminosities, but fades more rapidly. An average ejecta opacity of $\kappa_{\text{ej}} = 1.0 \text{ cm}^2 \text{ g}^{-1}$ is assumed for all parameters.

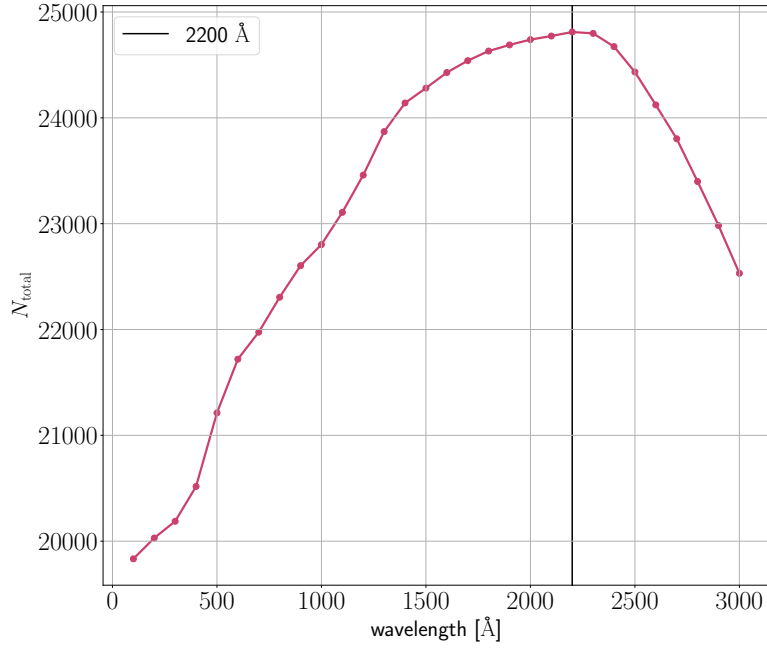


Figure 10. The total number of lines obtained from the ASD and Kurucz & Bell line lists for various threshold wavelengths. Because the ASD is more complete at only the very shortest wavelengths, a threshold of 2200 Å below which ASD lines are used and above which Kurucz lines are used is found to maximize the total number of lines.